Research Article | Vol. 32, No. 14 / 1 Jul 2024 / Optics Express 24072
Optics EXPRESS

Subwavelength and broadband on-chip mode splitting with shifted junctions

JACK HAINES,[1,*] POOJA UDAY NAIK,[1] KUNHAO JI,[1] VALERIO VITALI,[1,2] YOHAN FRANZ,[1] PERIKLIS PETROPOULOS,[1] AND MASSIMILIANO GUASONI[1]

[1]*Optoelectronics Research Centre, University of Southampton, Southampton, University Road West Highfield Campus B46, Southampton, SO17 1BJ, United Kingdom*
[2]*Electrical, Computer and Biomedical Engineering Department, University of Pavia, Pavia, 27100, Italy*
[*]*jh27g15@soton.ac.uk*

Abstract: We design and fabricate a sub-wavelength on-chip mode splitter based on the implementation of a shifted junction between a single-mode waveguide and a multimode waveguide. A proper choice of the device parameters enables to split the input beam into a combination of different guided modes of the multimode waveguide, minimizing radiation and reflection losses that amount to ~ 0.4 dB in our experiments. Because the splitting mechanism does not rely on phase-matching, we achieve broadband operation that could exceed 200 nm bandwidth (<0.5 dB splitting variation). This approach ensures temporal and phase synchronization among the output modes, with applications spanning from the emergent multimode photonics platform to traditional single-mode photonics operations.

1. Introduction

The successful developments of the last 20 years have positioned integrated photonics as one of the most promising routes for advancing telecom, quantum and mid-infrared technologies, paving the way for unprecedented innovations in data transmission and processing speed [1–3]. A fundamental operation in integrated photonics is the ability to manipulate the modal content [4]. This capability not only represents a crucial tool for the emerging multimode photonics platform [5–7], but also offers additional flexibility to traditional single-mode optics applications, from polarization control [8] to add-drop filters [9].

Several types of mode converters and splitters for on-chip generation and manipulation of higher-order modes have been proposed in the literature. Many of these are based on a $Nx1$ multiplexer device, where N beams from as many distinct single-mode waveguides are multiplexed into a multimode waveguide through multimode interference (MMI) devices [10,11], Y-junctions [12,13], directional couplers [14,15] or adiabatic structures [16,17]. Alternative solutions involve the conversion of a single mode beam into a pair of modes using non-standard Bragg gratings for fiber-to-chip coupling [18] or mode hybridization in tapered waveguide structures [19,20]. In recent years, a compact two-mode splitter solution has emerged for on-chip sensor applications. This approach utilizes a waveguide with a thickness step, fabricated through a double-layer lithography process, which excites both the fundamental and the first higher-order vertical mode [21,22].

The mentioned solutions typically face challenges such as complex fabrication, reliance on phase-matching conditions, or a large footprint, which restrict their useful bandwidth and integration.

#525394 https://doi.org/10.1364/OE.525394
Journal © 2024 Received 2 Apr 2024; revised 17 May 2024; accepted 29 May 2024; published 17 Jun 2024

Optics EXPRESS

In this work, we propose and demonstrate a mode splitter based on a laterally shifted junction between two waveguides with different widths and parallel but non-coincident axes. By adjusting three control parameters, namely the shift at the junction and the widths of the waveguides, we maximize the coupling to a specific combination of guided modes while minimizing at the same time reflection and radiation losses.

This solution boasts a virtually zero-footprint as it does not require additional supporting structures like MMI, tapers, Y-junctions, or directional couplers. Moreover, it provides broadband operation due to its phase-matching-free implementation. Finally, the simplicity of the design ensures a straightforward manufacturing process based on single-step deposition and etching, which minimises fabrication errors and brings excess losses down to ~0.4 dB.

We foresee that the proposed device could support both multimode and single-mode key operations. For example, parametric nonlinear processes in multimode waveguides typically involve synchronous excitation of $N>1$ modes [23–26], which may be hard to achieved through multiplexing solutions. In contrast, our solution decomposes one single beam into various spatial modes at the junction, ensuring temporal and phase synchronization among them. This versatility extends to essential single-mode applications such as power attenuation, power splitting, interferometric measurements and add-drop filters.

This paper is organised as follows: in Section 2 we introduce the splitter geometry and design; Section 3 covers the fabrication process and the experimental setup used for device characterisation; finally, in Section 4, we discuss the concluding remarks.

2. Design

The device under investigation consists of an input and an output rectangular waveguide connected via an abrupt junction, as represented in Fig. 1.

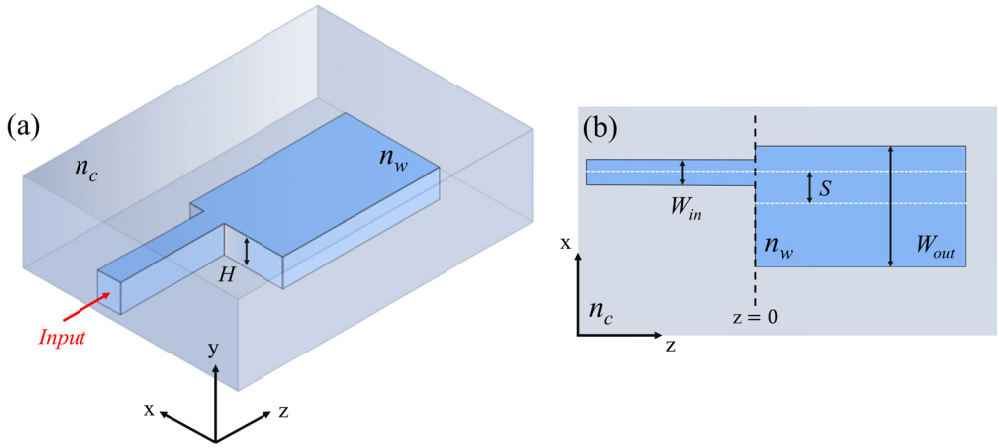

Fig. 1. Schematic of the mode splitter with shifted junction investigated and fabricated in this work. Panel (a): 3D view, H=thickness; n_w and n_c indicate the refractive index of the waveguide and of the cladding material, respectively. Panel (b): top view displaying the width W_{in} and W_{out} of the input and output waveguide, respectively, along with the lateral shift S between their corresponding longitudinal axes. The position z=0 indicates the position of the junction where mode splitting occurs.

The input waveguide supports the TE00 and TM00 modes, which can be selectively excited using a polarization controller, while the output waveguide is multimode. In this work, we consider the scenario where the TE00 mode is launched into the input waveguide. However, our analysis could be readily adapted to investigate the case of TM00 excitation. Let n_w and n_c

Optics EXPRESS

represent the refractive indices of the waveguide and the outer cladding materials, respectively; W_{in} and W_{out} the widths of the input and output waveguides, respectively; H their thickness and S the lateral shift along the transverse direction x at their junction. Light propagates from the input towards the output waveguide along the longitudinal direction z, where $z = 0$ indicates the junction position. In a reference system aligned with the input waveguide axis, we indicate respectively with $\mathbf{e}_{in}(x, y)$ and $\mathbf{h}_{in}(x, y)$ the electric and magnetic field of the guided mode in the input waveguide, whereas $\mathbf{e}_{out,p}(x - S, y)$ and $\mathbf{h}_{out,p}(x - S, y)$ denote the electric and magnetic field of the p-guided mode in the output waveguide.

At the junction, the input waveguide mode is partially transmitted, partly splitting into a combination of guided modes of the output multimode waveguide and partly radiating out. By adjusting the system parameters we can maximise the coupling to the desired modes of the output waveguide, and at the same time minimise radiation and reflection losses. It is worth noting that mode splitting occurs entirely at the junction, without the assistance of additional supporting structures, therefore the corresponding footprint is virtually null. We indicate with $P_m = |A_m|^2$ the fraction of input power coupled to the $m-$mode of the output waveguide as a result of the splitting, which is estimated through the following decomposition formula [27]:

$$A_m = \frac{\int_{xy} \mathbf{e}_{in}^{(t)}(x, y) \times \mathbf{h}_{out,m}^{*(t)}(x - S, y)dxdy}{2} + \frac{\int_{xy} \mathbf{h}_{in}^{(t)}(x, y) \times \mathbf{e}_{out,m}^{*(t)}(x - S, y)dxdy}{2} \tag{1}$$

with superscript (t) indicating the transverse component, and where the input and output guided modes are normalised such that their power (integral of the Poynting vector over the xy plane) is unitary. The quantity $P_{tr} = \sum_m P_m$ represents the overall fraction of input power transmitted and carried by the guided modes of the output waveguide, whereas the complementary $100\% - P_{tr}$ indicates the fraction of power which is either reflected or radiated out at the junction. Once the electric and magnetic fields of the guided modes are computed via a standard finite element method (FEM) solver (Comsol Multiphysics), Eq. 1 can be used for a fast tune of the system parameters.

In the following, we illustrate a significant example where the waveguides, fabricated in our cleanrooms, are made of silicon nitride (SiN) and are embedded in silica (SiO_2) cladding. The waveguide thickness, fixed by the deposition process, is $H = 300$ nm. We also fix the output waveguide width $W_{out} = 3$ μm, corresponding to a waveguide supporting 2 TM modes (TM00 and TM01) and 3 TE modes (TE00, TE01 and TE02). We use Eq. 1 to estimate the splitting ratios ($m = \{TM00, TM01, TE00, TE01, TE02\}$), which are displayed in Fig. 2 as a function of W_{in} and S. Several different splitting ratios can be achieved, and for a proper choice of W_{in} and S, we can suppress radiation and reflection losses (see in Fig. 2(d) where $P_{tr} \sim 100\%$). In all instances, the coupling to TM modes is negligible ($P_{TM00} \sim 0$, $P_{TM01} \sim 0$) as a result of the orthogonal polarization with respect to the TE00 mode of the input waveguide.

We now focus on a specific case where the splitting over the TE00 and TE01 modes of the output waveguide is identical, namely $P_{TE00} = P_{TE01}$, and the sum of their powers $P_{TE00} + P_{TE01}$ is maximized, thereby minimizing the contribution of the TE02 mode. This corresponds to a case of practical interest for nonlinear applications (see Conclusion section) and is achieved when $W_{in} = 825$ nm and $S = 775$ nm (see black dot in Fig. 2), which yields splitting ratios $P_{TE00} = P_{TE01} \sim 46\%$ and $P_{TE02} \sim 8\%$. Consequently $P_{tr} \sim 100\%$, and therefore radiation and reflection are suppressed. From Fig. 2 we also observe that these splitting ratios are robust against fabrication errors: indeed variations of the input width W_{in} up to ± 300 nm and of the shift S up to ± 100nm do not change significantly the splitting ratios.

Figure 3(a) displays a full 3D FEM simulation of Maxwell's equations in a device characterised by the above-mentioned dimensions. The corresponding evolution of the relative power of the modes into play, computed via mode decomposition [27], is reported in Fig. 3(b). We note that, as previously mentioned, the splitting process is not adiabatic but takes place entirely at

Optics EXPRESS

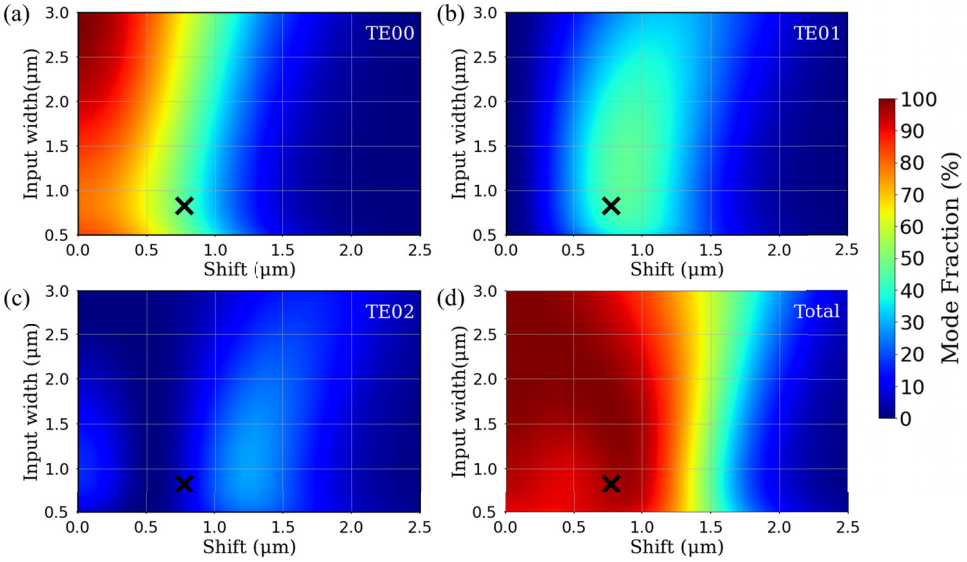

Fig. 2. Splitting ratios versus shift S and input waveguide width W_{in}, calculated via Eq. 1. Panels (a)-(b)-(c): relative powers P_{TE00}, P_{TE01} and P_{TE02}. Note that the power coupled over TM modes is negligible (therefore not reported here). The black crosses identify the case W_{in} = 825 nm and S = 775 nm, for which $P_{TE00} = P_{TE01} \sim 46\%$ and $P_{TE02} \sim 8\%$. Panel (d): total fraction of transmitted power $P_{tr} = P_{TE00} + P_{TE01} + P_{TE02}$ coupled to the output waveguide modes.

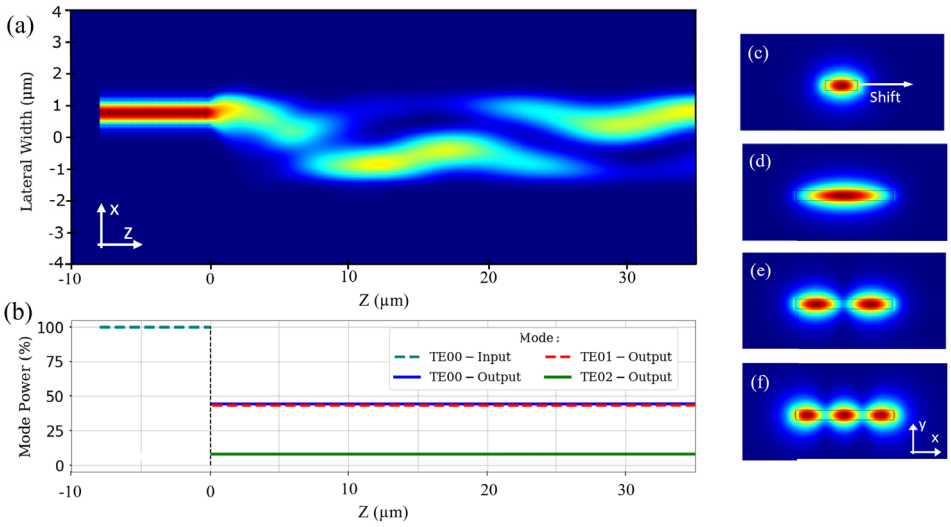

Fig. 3. Simulation results for the instance W_{in} =825 nm and S = 775 nm (a): finite-element-method (FEM) simulation illustrating the propagation of the input waveguide TE00 mode and the splitting at the shifted junction located at $z = 0$. (b): corresponding evolution of the power coupled to the waveguide modes. The power, initially coupled to the mode TE00 of the input waveguide ($z < 0$), is split at the junction ($z = 0$). After the splitting ($z > 0$), the power turns out to be coupled evenly to modes TE00 and TE01 of the output waveguide ($P_{TE00} = P_{TE01} = 46\%$), with a small fraction coupled to mode TE02 ($P_{TE02} = 8\%$). (c)-(f): transverse profiles of the modes into play: TE00 of the input waveguide (c); TE00 (d), TE01 (e) and TE02 (f) of the output waveguide.

Optics EXPRESS

the junction (z = 0). Moreover, at the junction output, the splitting ratios closely align with the estimation provided by Eq. (1), namely $P_{TE00} = P_{TE01} \sim 46\%$ and $P_{TE02} \sim 8\%$.

More in general, we have verified that the 3D FEM simulations and Eq. (1) agree across a wide range of parameters. This validates the latter and certifies its suitability for the rapid design of the mode splitter proposed in this work.

3. Fabrication and experiments

The mode splitter introduced in the previous section has been fabricated through the CORNERSTONE prototyping service based at the University of Southampton. The test device was manufactured on a silicon nitride-on-insulator wafer, starting from a 300 nm-thick silicon nitride layer deposited onto an 8-inch silicon wafer coated with a 3 μm-thick silicon dioxide layer. The structure was patterned with deep-ultraviolet (DUV) lithography. Subsequently, the patterned structure underwent an inductively coupled plasma (ICP) etching process, followed by the deposition of a 2 μm-thick silicon dioxide cladding layer. Finally, end facet polishing was carried out to optimize input and output coupling efficiency.

Alongside the mode splitter under analysis, illustrated in Fig. 4(a), two support structures were also fabricated to assess excess loss (EL) and mode splitting ratios at the device output. The first structure is a long adiabatic tapered waveguide, which serves as a reference waveguide for the measure of the EL induced by the shift junction. Its initial and final widths correspond to the widths of the input and output waveguides of the mode splitter, namely 825 nm and 3 μm, respectively. The second structure is a Y-branch device, illustrated in Fig. 4(b), where the upper branch features the original shifted junction, while the bottom branch incorporates both the shifted junction followed by an inverse taper, which is designed to allow the radiation of higher-order modes outside of the device (it supports the propagation of the TE00 mode only).

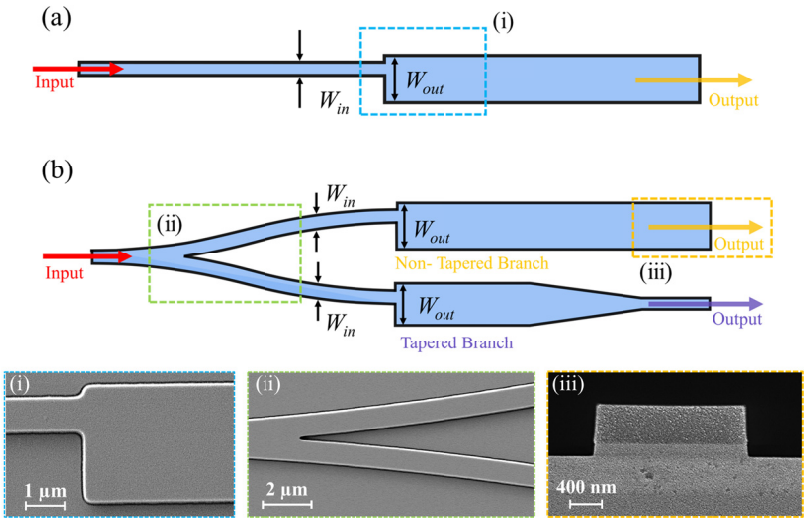

Fig. 4. Schematic of the devices fabricated and tested to implement free-space modal decomposition. (a): original mode splitter with shifted junction (note: this is the same as in Fig. 1). (b): Y-branch device. Both the top and bottom branches include the shifted-junction. Moreover, the bottom branch includes an output tapered section to radiate higher-order modes. Additional panels (i), (ii) and (iii) are, respectively, scanning-electron-microscope (SEM) images of the junction at the interface between the input and output waveguides, the bifurcation region in the Y-branch device and a cross section of the etched SiN layer for the top branch of the mode splitter before resist stripping and capping.

Optics EXPRESS

Note that the junctions in the structures under test are always in proximity to a chip edge, typically less than a few hundred micrometers apart. This ensures that within the pathway from the junction to the chip's output, where the power measurements are evaluated, there is negligible differential loss among the spatial modes. Otherwise, the accuracy of the splitting measurement could be compromised.

A schematic of the experimental setup for the characterisation of the fabricated devices is reported in Fig. 5. It is worth noting that while integrated gratings and multiplexers could be designed to assist input and output coupling as well as mode decomposition, however, these are typically characterised by a narrow bandwidth compared to the mode splitter under investigation. Therefore, to estimate the bandwidth of the device more accurately, we rely on free space optics as described below. A continuous wave (CW) tunable and narrow band diode laser with 10 dBm output power across the 1530-1610 nm spectral band serves as the optical source, which is coupled at the input facet of the devices via edge-coupling through a 60x, 0.85 NA objective. A polarisation controller (PC) and a linear polariser are used to control the polarization of the input beam. The chip including the devices under test is positioned on an XYZ piezoelectric stage for high-precision optical coupling. At the output facet, light is collected through a second 60x, 0.85 NA objective, and the corresponding power is measured with an optical power meter (OPM) with 1 nW resolution.

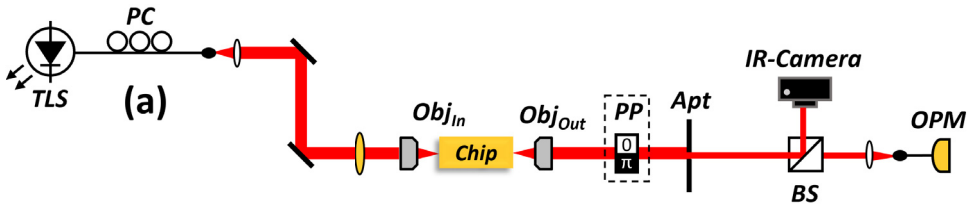

Fig. 5. Experimental setup. TLS = tunable laser source (1530 - 1610 nm); PC = polarisation controller; $Obj_{In,Out}$ = input/output objective; Apt = Aperture; BS = beam splitter; OPM = optical power meter. The phase plate *PP* is included when implementing free-space modal decomposition at the output of the mode-splitter of Fig. 4(a). It is otherwise removed when characterising the Y-branch of Fig. 4(b).

In the first set of measurements, we have estimated the EL of the device as the ratio between the average transmission in the mode splitter (Fig. 4(a)) and the average transmission in the reference waveguide. These averages were calculated from data collected across four different replicas of the devices under test, yielding an estimation of $EL \sim 0.4$ dB, i.e. $\sim 10\%$. We attribute EL mainly to reflection and radiation, hence resulting in the power coupled to the output guided modes being $P_{tr} \sim 90\%$. Furthermore, we have measured a polarization extinction ratio > 15 dB, which suggests a negligible coupling between the TE00 field of the input waveguide and the TM00 and TM01 modes of the output waveguide, confirming the numerical results reported in the previous section.

The second set of measurements involved mode decomposition at the output of the mode splitter of Fig. 4(a). Mode decomposition follows a standard procedure outlined in [28,29], which entails passing the beam collected at the output of the device through a free-space phase plate (PP) for TE00-to-TE01 (or TE01-to-TE00) mode conversion [30]. This is followed by the coupling to a single-mode fibre accurately aligned with the PP. The ratio between the power coupled to the single-mode fibre when the PP is aligned and when it is not aligned provides an estimate of the ratio P_{TE01}/P_{TE00}.

The last set of experiments has been carried out on the Y-branch structure of Fig. 4(b). The bottom branch is a replica of the top branch, but includes an inverse taper that allows radiation of the higher-order modes. Therefore, the ratio of the output power measured at the bottom and

Optics EXPRESS

the top branch provides an estimate of the power carried by the TE00 mode to the total guided transmitted power, namely P_{TE00}/P_{tr}. Finally, from the estimate of P_{TE00}/P_{tr} and of P_{TE01}/P_{TE00} previously introduced, we readily isolate the relative powers P_{TE00}, P_{TE01} and P_{TE02}.

The experimental results are summarized in Fig. 6, alongside those obtained from numerical simulations. We observe a good consistency between theoretical and experimental results within the limits of experimental error, which is calculated by averaging across 8 different measurements. While P_{TE00} is slightly larger (~6%) than P_{TE01}, their values are similar, while P_{TE02} turns out to be strongly suppressed as predicted by the theoretical results. Moreover, the splitting ratios exhibit small variations across different wavelengths, specifically < 0.5 dB for TE00 and TE01. This stems from the fact that mode splitting at the junction is primarily influenced by the spatial distribution of the modes (see Eq. 1), which remains relatively stable over a wide bandwidth when the input and output waveguide have appropriate dimensions. While the experiments are constrained within the 1530 - 1610nm operational band of the optical source, however, the numerical results span a broad spectral region and show a 0.5 dB variation bandwidth exceeding 200 nm. Therefore, unlike structures such as MMIs and directional couplers, the device under investigation operates without the constraints of phase matching, thus ensuring broadband operation.

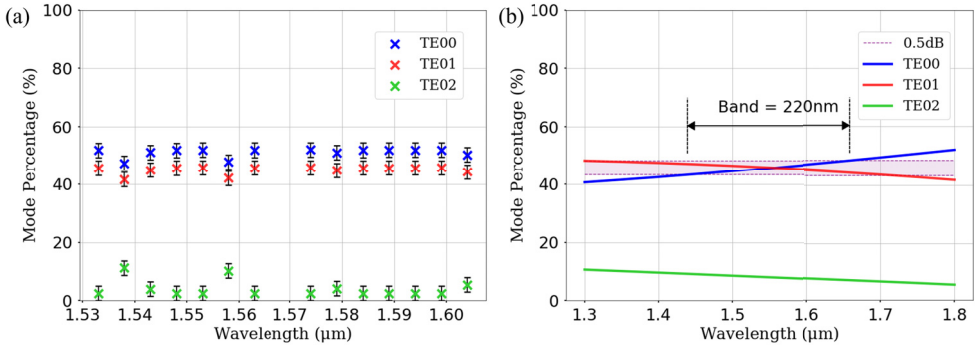

Fig. 6. Experimental and theoretical results. (a): Estimation of splitting ratios P_{TE00} (blue), P_{TE01} (red) and P_{TE02} (green) in the spectral band 1530 - 1610 nm from experimental measurements; (b): splitting ratios numerically calculated from finite-element-simulations. The shaded region indicates the 0.5 dB variation window, from which an operational bandwidth of ~220 nm was estimated.

As previously mentioned, because the splitting occurs at the interface between the two waveguides connected by the step junction, the footprint is virtually null. In practice, the size of the junction is defined by the sharpness of the edges at the interface between the input and output waveguides, specifically the transition length between them. This is typically a few tens to a few hundred nanometres (see Fig. 4(a)), and therefore sub-wavelength within the spectral region under analysis in this work.

4. Conclusion

In this work we have designed, fabricated and tested an integrated mode splitter based on a shifted junction between a single-mode and a multimode waveguide. This geometry enables efficiently coupling the input waveguide beam to a multitude of guided modes in the output waveguide, thereby enhancing coupling efficiency while minimizing radiation and reflection losses.

This phase-matching-free approach ensures broadband operation over a spectral window of several hundred nanometres. The splitting ratio between the output waveguide modes is adjusted through the system parameters, namely the input and output waveguide widths alongside the

Optics EXPRESS

lateral shift. Furthermore, the splitting occurs entirely at the junction and within a sub-wavelength range (tens to a few hundred nanometres), corresponding to the transition length between the input and the output waveguide, which is determined by the fabrication process. Consequently, the output waveguide modes are excited in phase and synchronized, and the junction footprint is $< 1\mu m^2$.

To assess our design, we have provided an example of an integrated mode splitter on a silicon nitride-on-insulator platform, which has been manufactured via standard DUV lithography and ICP etching. The output waveguide supports 3 TE modes, and the system is designed to maximize and equalize the coupling to the first two (TE00 and TE01) modes, while minimizing the coupling to the latter (TE02). The theoretical predictions are in good agreement with the experimental results, exhibiting an excess loss $\sim$ 0.4 dB and good spectral uniformity, with splitting variation $<$ 0.5 dB across the 1530 - 1610nm spectral band investigated in the experiments. In Table 1, we present a comparison between our device and other typical solutions for mode manipulation and generation. This allows us to highlight the distinct benefits of our solution, including its reduced footprint, wide bandwidth, along with phase and temporal synchronization.

Table 1. Comparison between state of the art solutions and this work. Here PTS = phase and temporal synchronisation, DC = directional coupler.

Reference	Device Type	Excess Loss (dB)	Footprint (μm^2)	Bandwidth (nm)	PTS
This work	Junction	0.4	<1	>100[a]	Yes
[14]	DC	0.3	50	100	No
[13]	Y-Branch	1	2	100	No
[17]	Adiabatic	0.4-0.75	200	180	No
[10]	MMI	1	60	>30	No

[a]Note: estimated bandwdith is up to 220 nm.

The mode splitter investigated in this work would benefit any application where controlled and synchronised excitation of different spatial modes is critical. An example is provided by Kerr parametric amplification in multimode waveguides, where an intense pump beam coupled to 2 distinct modes is converted to a Stokes and anti-Stokes wavelengths, each coupled respectively to one of the pump modes [24]. In this case, the parametric amplification is maximised when the pump beam is evenly coupled to the 2 modes [25], a condition satisfied by the mode splitter discussed in Section 3.

Beyond its applicability in multimode photonics, the proposed mode splitter may be used for implementing conventional on-chip single-mode operations. This includes a low-loss optical attenuator, with an attenuation factor defined by the power ratio between the fundamental mode of the output waveguide and the fundamental mode of the input waveguide. Furthermore, the ability to excite in-phase and synchronously a combination of different modes could extend the functionality of bimodal interferometers. Finally, we envisage that our mode splitter could contribute to the development of additional single-mode devices, including optical power splitters [31] or add-drop filters [9], leveraging higher-order modes to assist their implementation.

Funding. Engineering and Physical Sciences Research Council (EP/T019441/1); European Research Council (802682).

Disclosures. The authors declare no conflicts of interest.

Data availability. Data underlying the results may be obtained from the authors upon reasonable request.

References

1. J. Wang, F. Sciarrino, A. Laing, *et al.*, "Integrated photonic quantum technologies," Nat. Photonics **14**(5), 273–284 (2020).
2. S. Y. Siew, B. Li, F. Gao, *et al.*, "Review of silicon photonics technology and platform development," J. Lightwave Technol. **39**(13), 4374–4389 (2021).

Optics EXPRESS

3. H. Lin, Z. Luo, T. Gu, *et al.*, "Mid-infrared integrated photonics on silicon: a perspective," Nanophotonics **7**(2), 393–420 (2017).
4. C. Li, M. Zhang, H. Xu, *et al.*, "Subwavelength silicon photonics for on-chip mode-manipulation," PhotoniX **2**(1), 11 (2021).
5. I. Cristiani, C. Lacava, G. Rademacher, *et al.*, "Roadmap on multimode photonics," J. Opt. **24**(8), 083001 (2022).
6. D. J. Richardson, J. M. Fini, and L. E. Nelson, "Space-division multiplexing in optical fibres," Nat. Photonics **7**(5), 354–362 (2013).
7. L. G. Wright, W. H. Renninger, D. N. Christodoulides, *et al.*, "Nonlinear multimode photonics: nonlinear optics with many degrees of freedom," Optica **9**(7), 824–841 (2022).
8. D. Dai and H. Wu, "Realization of a compact polarization splitter-rotator on silicon," Opt. Lett. **41**(10), 2346–2349 (2016).
9. J. Jiang, H. Qiu, G. Wang, *et al.*, "Silicon lateral-apodized add–drop filter for on-chip optical interconnection," Appl. Opt. **56**(30), 8425–8429 (2017).
10. M. Ye, Y. Yu, J. Zou, *et al.*, "On-chip multiplexing conversion between wavelength division multiplexing–polarization division multiplexing and wavelength division multiplexing–mode division multiplexing," Opt. Lett. **39**(4), 758–761 (2014).
11. L. Han, S. Liang, H. Zhu, *et al.*, "Two-mode de/multiplexer based on multimode interference couplers with a tilted joint as phase shifter," Opt. Lett. **40**(4), 518–521 (2015).
12. W. Chen, P. Wang, T. Yang, *et al.*, "Silicon three-mode (de) multiplexer based on cascaded asymmetric y junctions," Opt. Lett. **41**(12), 2851–2854 (2016).
13. Z. Zhang, Y. Yu, and S. Fu, "Broadband on-chip mode-division multiplexer based on adiabatic couplers and symmetric y-junction," IEEE Photonics J. **9**(2), 1–6 (2017).
14. Y. Ding, J. Xu, F. Da Ros, *et al.*, "On-chip two-mode division multiplexing using tapered directional coupler-based mode multiplexer and demultiplexer," Opt. Express **21**(8), 10376–10382 (2013).
15. S. Mao, L. Cheng, C. Zhao, *et al.*, "Compact hybrid five-mode multiplexer based on asymmetric directional couplers with constant bus waveguide width," Opt. Lett. **48**(10), 2607–2610 (2023).
16. D. Guo and T. Chu, "Silicon mode (de) multiplexers with parameters optimized using shortcuts to adiabaticity," Opt. Express **25**(8), 9160–9170 (2017).
17. J. Wang, Y. Xuan, M. Qi, *et al.*, "Broadband and fabrication-tolerant on-chip scalable mode-division multiplexing based on mode-evolution counter-tapered couplers," Opt. Lett. **40**(9), 1956–1959 (2015).
18. I. Demirtzioglou, C. Lacava, A. Shakoor, *et al.*, "Apodized silicon photonic grating couplers for mode-order conversion," Photonics Res. **7**(9), 1036–1041 (2019).
19. A. Pan, C. Hu, C. Zeng, *et al.*, "Fundamental mode hybridization in a thin film lithium niobate ridge waveguide," Opt. Express **27**(24), 35659–35669 (2019).
20. D. Vermeulen, K. Van Acoleyen, S. Ghosh, *et al.*, "Efficient tapering to the fundamental quasi-tm mode in asymmetrical waveguides," in *15th European conference on Integrated Optics (ECIO 2010)*, (2010).
21. K. E. Zinoviev, A. B. González-Guerrero, C. Domínguez, *et al.*, "Integrated bimodal waveguide interferometric biosensor for label-free analysis," J. Lightwave Technol. **29**(13), 1926–1930 (2011).
22. A. Fernández Gavela, D. Grajales García, J. C. Ramirez, *et al.*, "Last advances in silicon-based optical biosensors," Sensors **16**(3), 285 (2016).
23. Y. Ding, J. Xu, H. Ou, *et al.*, "Mode-selective wavelength conversion based on four-wave mixing in a multimode silicon waveguide," Opt. Express **22**(1), 127–135 (2014).
24. S. Signorini, M. Mancinelli, M. Borghi, *et al.*, "Intermodal four-wave mixing in silicon waveguides," Photonics Res. **6**(8), 805–814 (2018).
25. M. Guasoni, "Generalized modulational instability in multimode fibers: Wideband multimode parametric amplification," Phys. Rev. A **92**(3), 033849 (2015).
26. V. Vitali, T. Domínguez Bucio, H. Liu, *et al.*, "Fully-integrated and broadband si-rich silicon nitride wavelength converter based on bragg scattering intermodal four-wave mixing," Photonics Res. **12**(3), A1–A10 (2024).
27. Y. Franz and M. Guasoni, "Compact 1× n power splitters with arbitrary power ratio for integrated multimode photonics," J. Opt. **23**(9), 095802 (2021).
28. C. Lacava, T. D. Bucio, A. Z. Khokhar, *et al.*, "Intermodal frequency generation in silicon-rich silicon nitride waveguides," Photonics Res. **7**(6), 615–621 (2019).
29. O. F. Anjum, M. Guasoni, P. Horak, *et al.*, "Polarization-insensitive four-wave-mixing-based wavelength conversion in few-mode optical fibers," J. Lightwave Technol. **36**(17), 3678–3683 (2018).
30. "HoloOr - Mode Converter," https://www.holoor.co.il/mode-converter/. Accessed: February 10, 2024.
31. J. Haines, V. Vitali, K. Bottrill, *et al.*, "Fabrication of 1× n integrated power splitters with arbitrary power ratio for single and multimode photonics," Nanophotonics **13**(3), 339–348 (2024).